Short-Wave Infrared Janus Metastructure With Multitasking of Wide-Range Pressure Detection and High-Resolution Biosensing Based on Photonic Spin Hall Effect

Jun-Yang Sui, Jia-Hao Zou, Si-Yuan Liao, Bao-Fei Wan, and Hai-Feng Zhang

***Abstract*— The photonic spin Hall effect (PSHE) is an effective measurement approach to characterize changes in pressure and weak refractive index. The metastructure based on a layered structure is equipped with the Janus feature by the asymmetric arrangement of different dielectrics. Electromagnetic waves (EWs) exhibit different electromagnetic characteristics when propagate from opposite directions of the metastructure within the short-wave infrared (SWIR) range. When EWs are incident positively at a frequency f of 260.87 THz ($\lambda = 1.15$ μm), a Janus metastructure (JM) based on PSHE can realize wide-range pressure detection (0–17.2 GPa) with the sensitivity (S) of 1.421°/GPa by using photoelasticity relation of the dielectrics. On the negative scale (EWs incident at $f = 128.39$ THz, that is $\lambda = 2.34$ μm), stomach cells, liver cells, epidermal cells, and their corresponding cancer cells can be clearly distinguished by the JM refractive index (RI) biosensing with the high resolution up to 1×10^{-6} RIU and S = 5.292×10^{-2} m/RIU. The multiscale and multitasking JM proposed not only makes up for the shortcomings of traditional single-scale and single-function sensors, but more importantly, the JM provides a new idea for the development of industrial production, healthcare, and biomedical fields, due to its excellent performance and real-time, label-free and noncontact detection.**

***Index Terms*— Biosensing, electromagnetic waves (EWs) propagation, Janus sensor, pressure detection, spin Hall effect.**

I. Introduction

SHORT-WAVE infrared (SWIR) spectroscopy is defined as frequencies of electromagnetic waves (EWs) ranging from 1.1 to 2.5 μm [1]. Most research on SWIR spectroscopy has focused on biological imaging [2] and probing biological tissue composition [3], utilizing its properties of reducing the fluorescence of tissues themselves and high spatiotemporal resolution [4]. In addition, due to the reduction of long-wave photon scattering, the optical sensors based on SWIR have the advantages of high penetration depth, noninvasive, and real-time detection [1], and their application in industrial production [5] and biomedical detection [6] has become a research hot spot in recent years. The photonic spin Hall effect (PSHE) can be considered as the optical version of the electronic spin Hall effect. In PSHE, the refractive index (RI) gradient and spin photon are analogous to the potential gradient and spin electron of the electronic spin Hall effect, respectively [7], [8]. PSHE appears as spin-dependent lateral displacement and splitting of the left-handed and right-handed circularly polarized components belonging to the linearly polarized beam reflected or refracted at the interface between two dielectrics [9], [10], which can be attributed to the spin-orbit coupling between the photonic spin (polarization) and the beam trajectory (orbital angular momentum) [9], [10]. Spin migration in PSHE is very sensitive to small changes in the physical parameters of the system, so PSHE can be used as an effective metrological tool to characterize changes in pressure and weak RI [11]. Fortunately, Hosten and Kwiat [12] proposed a weak measurement technique, which could magnify the PSHE phenomenon observed in the experiment by nearly 10^4 times, making it more convenient to observe and measure changes in physical quantities. In recent years, researchers have found that implementing PSHE in the SWIR range can facilitate sensitive, high-resolution, and real-time detection of changes in physical quantities that are small and difficult to measure directly. Popescu et al. [13] designed a three-layer waveguide plasma sensor that used PSHE to detect the magnetic field intensity of magnetic fluid in real time at a wavelength of 1.557 μm, with an optimal resolution of 7.81×10^{-8} Oe, which was much finer than the existing related technologies. Srivastava et al. [14] reported the sensitive detection of biomolecules by surface plasmonic resonance SWIR sensor based on PSHE, with sensitivity (S) reaching 1.555×10^5 μm/RIU (RIU is the unit of RI). Therefore, the sensor combining PSHE and SWIR has a certain research value.

Pressure sensors have been widely used in fields ranging from the automotive and aerospace industries to healthcare, such as mechanical manufacturing, air pressure monitoring, and motion monitoring [15], [16], [17]. Microsensors are preferred in many cases because the impact on the system under test is minimal. Hence, the Janus metastructure (JM)

Manuscript received 1 October 2023; revised 1 November 2023; accepted 14 November 2023. Date of publication 1 December 2023; date of current version 21 December 2023. The Associate Editor coordinating the review process was Xiangchen Qian. *(Corresponding author: Hai-Feng Zhang.)*

The authors are with the College of Electronic and Optical Engineering & College of Flexible Electronics (Future Technology), Nanjing University of Posts and Telecommunications, Nanjing 210023, China (e-mail: hanlor@163.com; hanlor@njupt.edu.cn).

This article has supplementary downloadable material available at https://doi.org/10.1109/TIM.2023.3338669, provided by the authors.

Digital Object Identifier 10.1109/TIM.2023.3338669

based on a layered structure in this article, which can detect pressure, has attracted much attention due to the advantages of small size and compact structure [18], [19]. In the last few years, Gowda et al. [20] designed a 1-D silicon photonic crystal pressure sensor to detect hydrostatic pressure in the range of 10–20 KPa by observing the wavelength shift of the resonant peak, with the S of 350 nm/GPa and the quality factor (Q) of 40 104. Suthar and Bhargava [21] used strain-sensitive quantum structure photonic crystals to realize pressure sensing of 0–6 GPa, with S and figure of merit (FOM) of 6.74 nm/GPa and 872.43 GPa^{-1}, respectively. Elsayed et al. [22] used polymer defect-based 1-D photonic crystals with micrometer device size to achieve pressure detection of 0–3 GPa in the range of SWIR, S = 21.16 THz/GPa. Although the detection performance of the above research works is very high, the scope of the pressure detection is narrow, which results in the application in the field of heavy machinery manufacturing being limited. Therefore, under the condition of ensuring good detection performance, pressure sensors with a wider pressure detection range can better serve the industrial field, which is urgently needed. Studies have shown that before the invasion of cancer cells, due to the increase of chromatin, the nuclear volume will increase and the RI will be higher than that of normal cells [23]. Therefore, the RI of cells may be an early identification indicator of cancer cells. Last several years, the design of biosensors for cancer cell detection based on RI differences has become a research hot spot. Ehyaee et al. [24] reported an RI sensor based on two-core photonic crystal fiber. The difference of RI in response to transmission spectrum could be used to detect six different types of tumor cells (Basal cell cancer, cervical cancer HeLa cells, Jurkat cancer cell, PC12 cancer cell, MDA-MB-231 breast cancer cell, and MCF-7 breast cancer cell), with a maximum resolution of 8×10^{-6} RIU [24]. Singh et al. [25] realized a highly angular sensitive surface plasmon resonance RI sensor to detect cancerous cells in the skin, cervix, and blood through changes in the absorption spectrum. The corresponding angular S values were 252.2, 305.7, and 319.46°/RIU. Compared with these RI biosensors, which determine the corresponding detected physical quantity through the observation of spectrum changes, the detection performance of using the PSHE displacement to determine the change of a weak physical quantity is less affected by external factors, such as noise, ambient light, and so on [26], [27]. Although the above sensors have excellent detection performance, unfortunately, their detection function is single and cannot achieve multiscale and multitasking. Focusing on improving a single function performance of the sensor inevitably limits the research ideas. Zhang et al. [28] proposed a multitasking sensor based on rectangular lattice photonic crystal fiber, which could measure strain, pressure, temperature (T_0), and curvature with S of 2.92 pm/$\mu\varepsilon$, 11.15 nm/MPa, 466.18 pm/K, and 339.85 pm/m^{-1}, respectively. It provides a new idea for the development of the sensor field. The multiscale and multitasking sensors are more suitable for applications in multiple scenarios, and function integration means high-cost performance.

TABLE I
MULTITASKING DETECTION PERFORMANCE OF THE JM

Scale	Detection	Performance	
Positive	Pressure detection	Range	0~17.2 GPa
		S	1.421 °/GPa
Negative	RI detection	Range	1.6595~1.6615
		S	5.292×10^{-2} m/RIU
		Resolution	1×10^{-6} RIU

In this article, an SWIR JM based on PSHE, which consists of a layered structure composed of different dielectrics, is proposed. The asymmetric arrangement of different dielectrics brings the metastructure Janus property, which means that EWs propagate at different SWIR wavelengths in the positive and negative directions, and different electromagnetic characteristics are presented [29], so they can meet the realization of multitasking with different performances (Table I shows the multitasking performance of JM on multiscale, and a detailed description will be discussed in Section III of this article). Under the condition that EWs incident at the frequency $f = 260.87$ THz ($\lambda = 1.15$ μm) on the positive scale, the JM can realize 0–17.2 GPa wide-range pressure detection with S = 1.421°/GPa by finding the incident angle θ of the PSHE displacement peak, which is rarely reported. When EWs of $f = 128.39$ THz ($\lambda = 2.34$ μm) propagate from a negative direction, RI biosensing in the range of 1.6595–1.6615 can be achieved by the JM with $S = 5.292 \times 10^{-2}$ m/RIU based on identifying the peak value of PSHE displacement at a fixed θ. What is more, since the JM has a resolution of up to 1×10^{-6} RIU for RI changes, RI detection with such high resolution can fully distinguish stomach cells (GES-1), liver cells (LO_2), epidermal cells (HEM) and the corresponding gastric cancer cells (MGC-803), liver cancer cells (7721), and epidermal cancer cells (MEL) by RI differences (1×10^{-4} RIU) [23]. The idea of wavelength division multiplexing is also reflected by using different EW wavelengths on the positive and negative scales, and beams with λ of 1.15 and 2.34 μm can be generated by laser sources [30], [31]. The given JM based on PSHE operates in the SWIR range allowing for high penetration depth, noninvasive, and real-time detection. In addition, the advantage of the JM to achieve multitasking on multiscale is a supplement to traditional single-scale and single-function sensors, and the JM proposed has certain application prospects in industrial production, healthcare, and the biomedical field. It should be emphasized that this work focuses on theoretical verification, so how to verify in experiments is not within the scope of this work since we do not have the experimental equipment and the funding.

II. THEORETICAL MODEL

The layered structure constituting JM is shown in Fig. 1. The detection cavity (represented by dielectric C) is inserted in the structure of the quasi-periodic arrangement of dielectrics gallium arsenide (GaAs) and silicon (Si) (symbolized by dielectrics A and B, respectively), which are represented by different colors [32]. The entire structure arranged along

TABLE II
PHOTOELASTICITY CONSTANTS OF THE GAAS AND SI UNDER EWS WAVELENGTH $\lambda = 1.15\ \mu$m [32]

Dielectric	n_0	p_{11}	p_{12}	C_1 (10^{-12}/Pa)	C_2 (10^{-12}/Pa)
GaAs	3.43	-0.165	-0.140	-18.39	-10.63
Si	3.42	-0.101	0.0094	-11.35	3.65

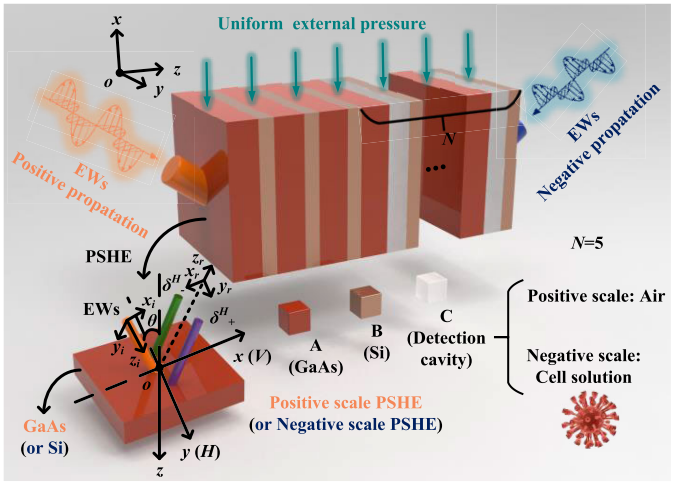

Fig. 1. Schematic of the JM layered structure, which consists of an asymmetrical arrangement of different dielectrics filled with various colors. The overall structure is $(AB)^3(ACB)^N$, where $N = 5$. The positive and negative propagation EWs are represented by orange and blue lines, respectively, and the incidence angle is θ. In addition, the incident EWs separately produce the PSHE phenomenon at the first dielectric interface on the positive or negative scale.

the $+z$-axis is $(AB)^3(ACB)^N$, where the period number is $N = 5$. The entire structure is simple in construction and easy to manufacture by the etching method (see Section I of Supplementary Material) [33]. To adapt to general conditions, the whole JM is exposed to air and works at room temperature $T_0 = 298$ K. The thicknesses of dielectrics A, B, and C are $d_A = 17$, $d_B = 40$, and $dc = 30$ nm, respectively, which proves the JM of compact structure and small size [18], [19]. The orange and blue lines (see Fig. 1) are used to separately symbolize the EWs incident into the JM in the positive and negative directions, respectively.

When a uniform external pressure (shown by the green arrow in Fig. 1) is applied vertically to the JM surface, the RI of the GaAs and Si will change under the influence of photoelasticity [32], [34]. Mathematically, the relationship between the applied pressure (σ) and RI of a material is expressed as follows [32], [34]:

$$\begin{pmatrix} n_{xx} \\ n_{yy} \\ n_{zz} \\ n_{yz} \\ n_{xz} \\ n_{xy} \end{pmatrix} = \begin{pmatrix} n_{xx} \\ n_{yy} \\ n_{zz} \\ 0 \\ 0 \\ 0 \end{pmatrix} - \begin{pmatrix} C_1 & C_2 & C_2 & 0 & 0 & 0 \\ C_2 & C_1 & C_2 & 0 & 0 & 0 \\ C_2 & C_2 & C_1 & 0 & 0 & 0 \\ 0 & 0 & 0 & C_3 & 0 & 0 \\ 0 & 0 & 0 & 0 & C_3 & 0 \\ 0 & 0 & 0 & 0 & 0 & C_3 \end{pmatrix} \begin{pmatrix} \sigma_{xx} \\ \sigma_{yy} \\ \sigma_{zz} \\ \sigma_{yz} \\ \sigma_{xz} \\ \sigma_{xy} \end{pmatrix}. \quad (1)$$

In (1), the stress-optical constant C_j ($j = 1$, 2, and 3) has the following relation [32], [34]:

$$C_1 = \frac{n_0^3(p_{12} - 2Vp_{11})}{2E} \quad (2)$$

$$C_2 = \frac{n_0^3[(p_{12} - V(p_{11} + p_{12})]}{2E} \quad (3)$$

$$C_3 = \frac{n_0^3 p_{44}}{2G} \quad (4)$$

where G, E, and V are Shear's modulus, Young's modulus, and Poisson's ratio, respectively [32], [34]. The values of the corresponding coefficients are provided in Table II. For isotropic crystals [32], [34]

$$p_{44} = \frac{(p_{11} - p_{12})}{2} \quad (5)$$

$$C_3 = \frac{E}{2(1+V)} \quad (6)$$

where p_{11}, p_{12}, and p_{44} are strain optical constants, representing the optical response of the material when it receives tensile strain along the principal stress axis, transverse strain along the principal stress axis, and shear strain along the shear stress direction, respectively [32], [34].

Using σ_{mn} to represent that the direction of the pressure applied is parallel to the mn plane, and n_{mn} is the corresponding change in dielectric RI [32], [34]. When σ is exclusively applied in a single direction (only cases perpendicular to the plane of the layered structure are considered), the entire device is under stress. As a result [32], [34]

$$\sigma_{xx} = \sigma_{yy} = \sigma_{zz} = \sigma \quad (7)$$

$$\sigma_{xy} = \sigma_{yz} = \sigma_{zx} = 0. \quad (8)$$

Therefore, (1) can be rewritten as [32], [34]

$$n_i = n_0 - (C_1 + 2C_2)\sigma \quad (9)$$

where n_0 is zero pressure (0 GPa) and n_i (i is denoted by A or B) is the RI of GaAs and Si.

The detection cavity is arranged in the JM structure and its role is to place the solution for biosensing. When the JM performs pressure detecting on the positive scale, the detection cavity is filled with stable air ($n_C = 1$). Under the condition of negative incidence of EWs, the cell solution to be detected, whose size is compressed by adopting the method of cell squeezing [35], [36], is injected into the detection cavity through a precise technique based on microinfiltration technology by hollow submicrometer-size pipettes [37]. The JM can distinguish between normal cells and cancer ones based on PSHE.

Also displaced in Fig. 1 is the PSHE phenomenon at the dielectric interface generated by a sufficiently narrow Gaussian beam with a certain θ on a positive or negative scale. The purple and green beams separately (see Fig. 1) represent the left-handed and right-handed circular polarization components, which are reflected at the interface. It can be expressed as a local wave packet with an arbitrarily narrow spectrum [38]

$$\tilde{E}_{i\pm} = (e_{ix} + \mathrm{i}oe_{iy})\frac{\omega_0}{\sqrt{2\pi}} \exp\left[-\frac{\omega_0^2\left(k_{ix}^2 + k_{iy}^2\right)}{4}\right] \quad (10)$$

where ω_0 symbolizes the beam waist and o is the polarization operator. k_{ix} and ki_y belong to the wave vector components in the x_i and y_i directions, respectively. $o = 1$ and $o = -1$ separately represent left-handed and right-handed circularly polarized beams. H and V are used to represent the horizontal and vertical polarization states, set along the $+y$-axis and $+x$-axis (as shown in Fig. 1). To obtain the reflected field, the relationship between the incident field and the reflected field is necessary to establish [38]

$$\begin{bmatrix} \tilde{E}_r^H \\ \tilde{E}_r^V \end{bmatrix} = \begin{bmatrix} r^p & \dfrac{k_{ry}\cot\theta_i(r^p + r^s)}{k_0} \\ -\dfrac{k_{ry}\cot\theta_i(r^p + r^s)}{k_0} & r^s \end{bmatrix} \begin{bmatrix} \tilde{E}_i^H \\ \tilde{E}_i^V \end{bmatrix}. \tag{11}$$

where k_0 is a representation of the free space wavenumber, and k_{ry} is the wave vector of the reflected light beam in the y_r direction. $\cot(x)$ is a cotangent function. Fresnel reflection coefficients belonging to the s and p waves are written as r^s and r^p (see Section II of Supplementary Material for detailed calculations), where the electric field vectors for s and p waves are separately set along $+y$-axis and $+x$-axis. According to (10) and (11), the expression of the reflection angle spectrum can be obtained [38]

$$\tilde{E}_r^H = \frac{r^p}{\sqrt{2}}\left[\exp\left(+ik_{ry}\delta_r^H\right)\tilde{E}_{r+} + \exp\left(-ik_{ry}\delta_r^H\right)\tilde{E}_{r-}\right] \tag{12}$$

$$\tilde{E}_r^V = \frac{ir^s}{\sqrt{2}}\left[-\exp\left(+ik_{ry}\delta_r^V\right)\tilde{E}_{r+} + \exp\left(-ik_{ry}\delta_r^V\right)\tilde{E}_{r-}\right] \tag{13}$$

where $\delta_r^H = (1 + r^s/r^p)\cot\theta_i/k_0$ and $\delta_r^V = (1 + r^p/r^s)\cot\theta_i/k_0$. $\tilde{E}_{r\pm}$ can be written in a similar style to (10). For reflected light, the lateral displacement of the two spin components of PSHE can be given [38]

$$\delta_\pm^H = \mp\frac{\lambda}{2\pi}\left[1 + \frac{|r^s|}{|r^p|}\cos(\varphi^s - \varphi^p)\right]\cot\theta_i \tag{14}$$

$$\delta_\pm^V = \mp\frac{\lambda}{2\pi}\left[1 + \frac{|r^p|}{|r^s|}\cos(\varphi^p - \varphi^s)\right]\cot\theta_i. \tag{15}$$

In this article, we only discuss the displacement δ_+^H of the left circular polarization component belonging to PSHE under horizontal polarization [38]

$$\delta_+^H = -\frac{\lambda}{2\pi}\left[1 + \frac{|r^s|}{|r^p|}\cos(\varphi^s - \varphi^p)\right]\cot\theta_i. \tag{16}$$

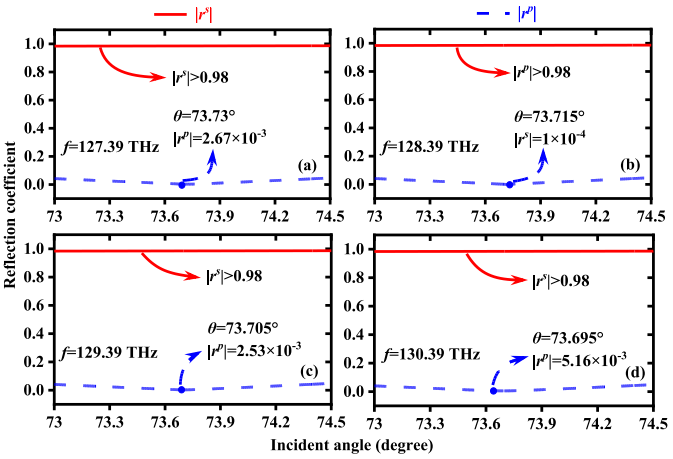

Fig. 2. Fresnel reflection coefficient curves of $|r^s|$ and $|r^p|$ under different incident frequencies. (a) $f = 127.39$ THz. (b) $f = 128.39$ THz. (c) $f = 129.39$ THz. (d) $f = 130.39$ THz.

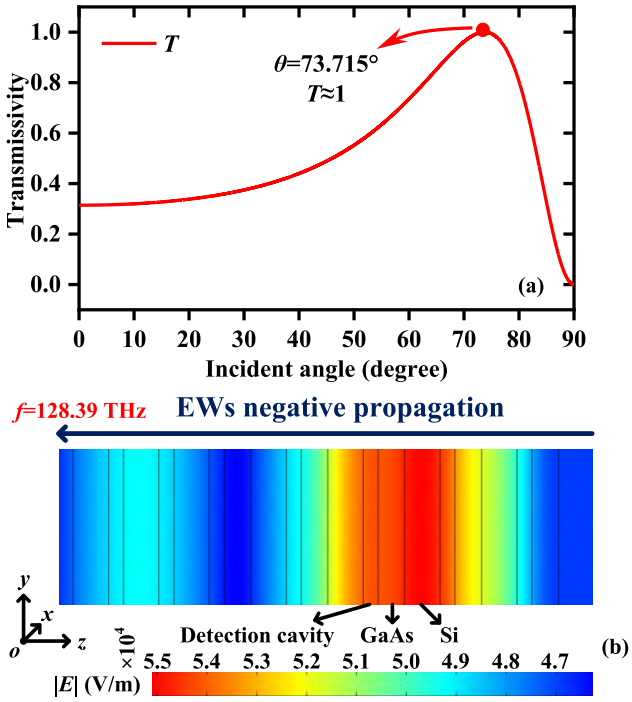

Fig. 3. Simulation results when the EWs propagate negatively at the frequency of 128.39 THz. (a) Curve of T corresponds to the p wave. (b) Electric field energy distribution diagram of p wave propagation under the condition of $f = 128.39$ THz and $\theta = 73.715°$.

III. Analysis and Discussion of Performances

To clearly clarify the δ_+^H peak generation principle and the incident EWs frequency selection, the case of EWs incident at different frequencies f on the backward scale and the detection cavity RI (n_C) fixed at 1.6615 is selected. The f values of 127.39, 128.39, 129.39, and 130.39 THz are selected at equal intervals of 1 THz. Since the effective RI and impedance of the overall layered structure have different electromagnetic responses to EWs of different frequencies, the wave vector and phase of the propagation EWs are affected [39]. This is reflected in the reflection coefficient, as shown in Fig. 2. Fig. 2(a)–(d) is the relationship between the Fresnel reflection coefficient curves $|r^s|$, $|r^p|$ (respectively, symbolized by red solid lines and blue dashed lines, respectively), and θ. It is found that $|r^s|$ is always greater than 0.98 within $\theta = 73°$–$74.5°$, but at a certain θ, $|r^p|$ is falling fast and reaches the minimum, and the lowest values of $|r^p|$ are 2.67×10^{-3}, 1×10^{-4}, 2.53×10^{-3}, and 5.16×10^{-3} corresponding to 127.39, 128.39, 129.39, and 130.39 THz, respectively.

To explore the physical principle of $|r^p|$ rapidly drops to 1×10^{-4} at $\theta = 73.715°$ [as shown in Fig. 2(b)], the reflection gap is analyzed first. Fig. 3(a) gives the graph of transmittance (T) and θ under the p wave propagation. It is obvious that there is a T peak with T approximately 1 at $\theta = 73.715°$.

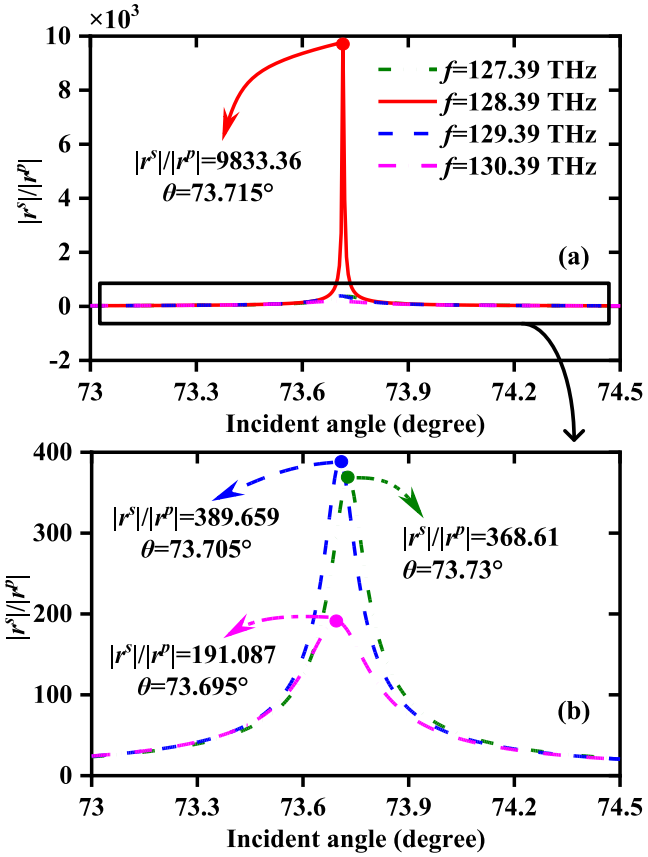

Fig. 4. Schematics of (a) $|r^s|/|r^p|$ corresponding to different f values and (b) enlarged image.

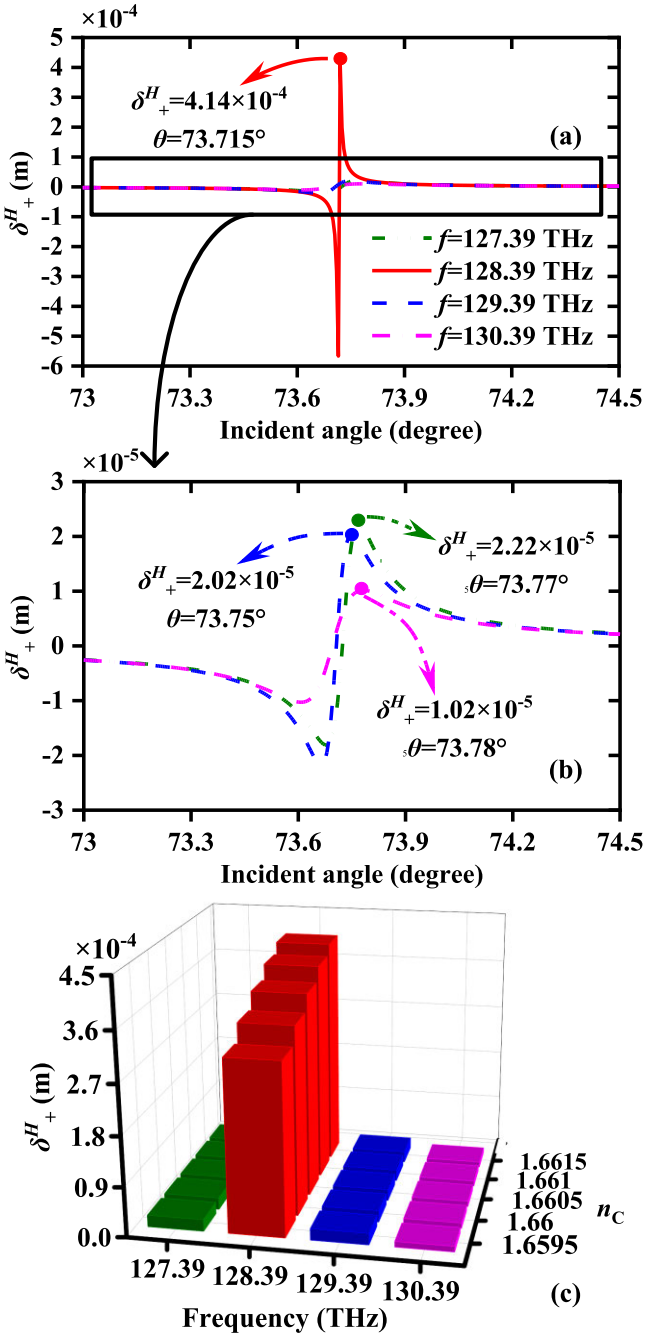

Fig. 5. When EWs are incident from the negative direction at different f values. (a) Comparison plots of δ_+^H. (b) Enlarged image. (c) Plots of δ_+^H peak values under different n_C values.

The distribution diagram of electric field energy in Fig. 3(b) is given to explain this phenomenon. In the case of p wave incident from the negative direction at $f = 128.39$ THz and $\theta = 73.715°$, the electric field is localized and enhanced in the defect layers: detection cavity, GaAs, and Si layers. Therefore, the located defect mode resonance, which means that the resonance peak caused by the electric field localization after the introduction of defects is formed [40], [41], is excited. So, a high-value T peak is generated [41], resulting in a reflection gap, which leads to $|r^p|$ decreases rapidly.

According to (16), it can be seen that the size of PSHE displacement δ_+^H mainly depends on the $|r^s|/|r^p|$ part. Therefore, if the value of $|r^s|$ is constant, the smaller the value of $|r^p|$, the larger δ_+^H will be. In addition, Section III of the Supplementary Material explains the reason why the value of δ_+^H cannot go to infinity at the Brewster angle θ_B. Fig. 4 shows the curves of $|r^s|/|r^p|$ under different f values of incident EWs. It is found that when $f = 128.39$ THz, the peak value of $|r^s|/|r^p|$ at $\theta = 73.715°$ can reach 9833.36, much higher than that at other f, which is consistent with Fig. 2(b) having the lowest $|r^p|$ value compared to the other f. As exhibited in Fig. 5(a) and (b), $|r^s|/|r^p| = 9833.36$ lays the theoretical foundation for the peak value of δ_+^H reaches 4.14×10^{-4} m under $f = 128.39$ THz, which is much higher than other f cases with δ_+^H peak values of 2.22×10^{-5}, 2.02×10^{-5}, and 1.02×10^{-5} m [42], [43]. Fig. 5(c) shows the variation of δ_+^H peak value with n_C at different f values. It is clearly found that the δ_+^H peak value at $f = 128.39$ THz is significantly higher than that in other cases, and it changes significantly with the change of n_C. Since the proposed JM achieves biosensing by identifying the δ_+^H peak value on the negative scale, the choice of EWs with $f = 128.39$ THz can obtain better detection performance and is more convenient to observe in practice.

Microsensors with wide-range pressure detection are urgently needed in modern industrial manufacturing and medical care [15], [17]. When EWs are incident at $f = 260.87$ THz from the positive direction, through finding the θ

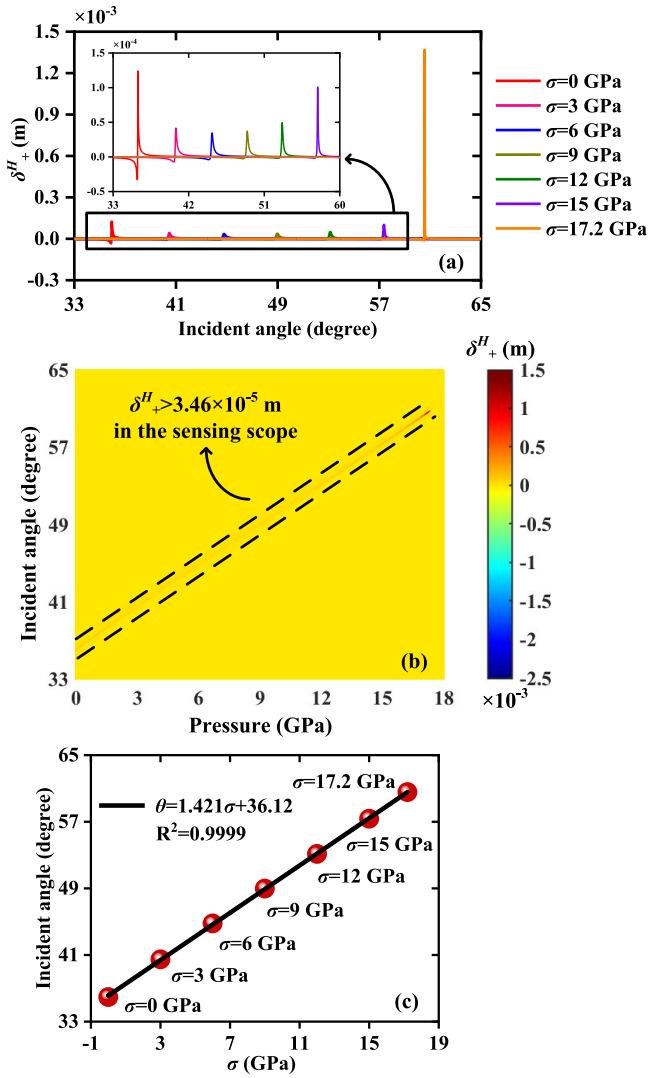

Fig. 6. Schematics of the pressure detection on the positive scale. (a) δ_+^H peaks belonging to different σ values. (b) Continuous change of δ_+^H peaks. (c) LFR between θ and σ.

TABLE III

RI VALUES BELONG TO DIFFERENT TYPES OF NORMAL AND CANCER CELLS UNDER THE 4.48×10^5 CELLS/ML DENSITY [23]

State	Type	RI (RIU)
Normal	GES-1	1.65998
	LO_2	1.66013
	HEM	1.66034
Cancer	MGC-803	1.66104
	7721	1.66069
	MEL	1.66124

belonging to the δ_+^H peak, the proposed JM is able to achieve pressure detection in the range of 0–17.2 GPa with the detection cavity filled with air ($n_C = 1$). In the 0–17.2-GPa detection range, σ test points are taken at 0, 3, 6, 9, 12, 15, and 17.2 GPa. Fig. 6(a) shows the relationship curve between δ_+^H and θ corresponding to each σ. As σ increases, the corresponding δ_+^H peak moves in the direction of greater θ and has the relevant θ of 35.95°, 40.475°, 44.785°, 48.975°, 53.14°, 57.365°, and 60.565°. The δ_+^H peaks belonging to

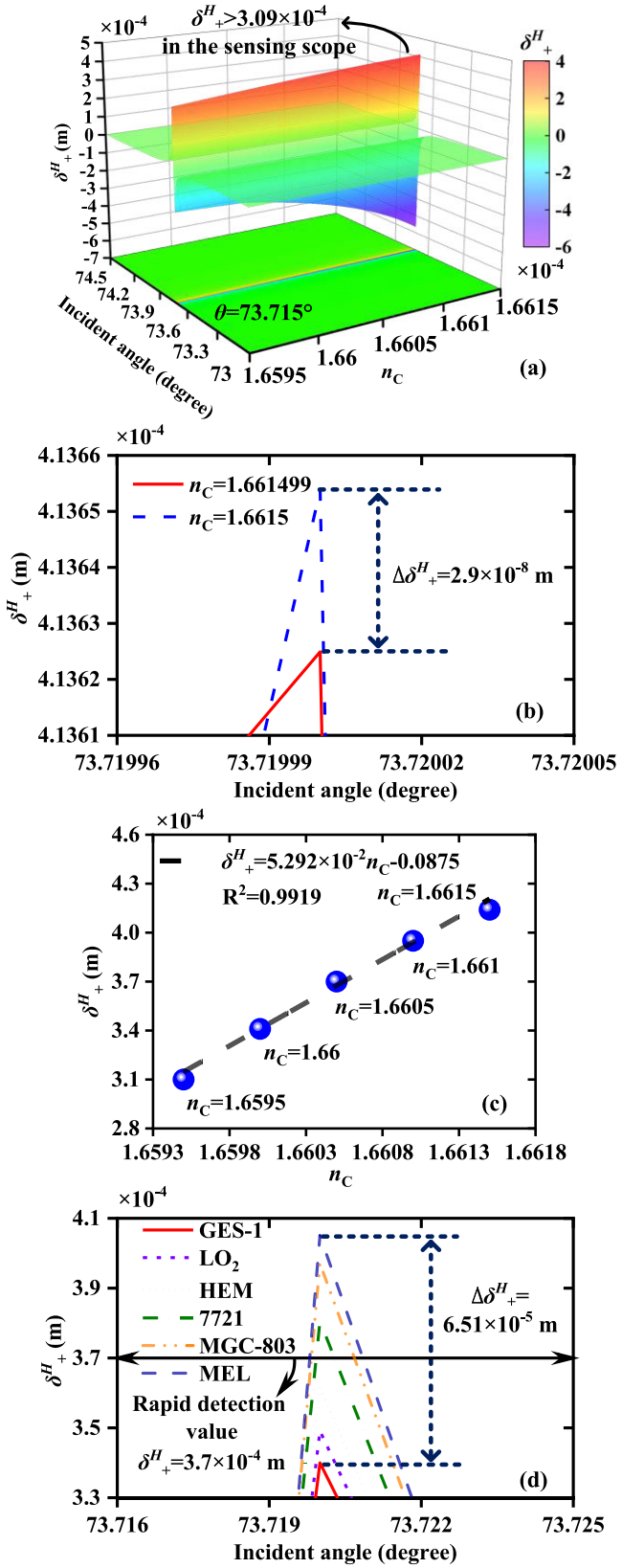

Fig. 7. Schematics of the RI detection on the negative scale. (a) Continuous change of δ_+^H peaks. (b) δ_+^H curves correspond to $n_C = 1.661499$ and $n_C = 1.6615$. (c) LFR between δ_+^H and n_C. (d) δ_+^H peaks belong to different normal cells and cancer ones.

$\sigma = 0$ and $\sigma = 17.2$ GPa have a θ difference of 24.615°, and δ_+^H peaks are sensitive to the changes in σ. This is because according to (9), the RI (n_A and n_B) of GaAs and Si is

TABLE IV
PUBLISHED REPORTS COMPARED WITH THE JM PROPOSED IN TERMS OF THE PERFORMANCE

Refs.	Years	Multiscale	Multitasking	Physical quantities	Detection performance	
[22]	2021	×	×	σ	Range	0~3 GPa
					S	21.16 THz/GPa
[21]	2021	×	×	σ	Range	0~6 GPa
					S	6.74 nm/GPa
[23]	2022	×	×	Normal and cancer cells	Range	1.6599~1.6611
					S	2.48×10^{-5} m/mL
					Resolution	1×10^{-5} RIU
[45]	2018	×	×	Cancer cells	Range	1.32~1.4
					S	720 nm/RIU
					Resolution	1×10^{-3} RIU
This work	2023	√	√	σ	Range	0~17.2 GPa
					S	1.421 °/GPa
				Normal and cancer cells	Range	1.6595~1.6615
					S	5.292×10^{-2} m/RIU
					Resolution	1×10^{-6} RIU

affected by the magnitude of applied pressure [32], [34], thus altering the effective RI of the entire layered structure, which will affect the displacement curve of PSHE [39]. To more intuitively observe the variation trend of the δ_+^H curve with the increase of σ, Fig. 6(b) presents a 3-D graph of the δ_+^H change when σ varies continuously at intervals of 0.01 GPa within the range of $\sigma = 0$–17.2 GPa. It can be seen that the δ_+^H peak decreases first and then rises with the increase of σ, which is consistent with Fig. 6(a). Moreover, in the σ range of 17.2–18 GPa, there are no obvious PSHE δ_+^H peaks that can meet the detection conditions. At the same time, in the σ detection range, the δ_+^H peak values are greater than 3.46×10^{-5} m, and the PSHE phenomenon can be easily observed experimentally by a measurement technique amplified 10^4 times [12]. To show the detection performance of the JM more clearly, corresponding to the detection points in Fig. 6(a), the linear fitting relationship (LFR) is obtained by using the linear fitting method. Fig. 6(c) displays the LFR of θ and σ belonging to δ_+^H peaks, $\theta = 1.421\sigma + 36.12$. 1.421°/GPa is S, reflecting the sensitive response of the JM to changes in σ. R^2 is used to evaluate the quality of linear fitting, and $R^2 = 0.9999$ indicates that the JM pressure detection is reliable. Moreover, $\text{arccot}(-2\pi\delta_+^H/(\lambda(1 + \cos(\varphi^s - \varphi^p)|r^s|/|r^p|)) = 1.421(n_0 - n_i)/(C_1 + 2C_2) + 36.12$ is the closed form equation for θ of δ_+^H peak and σ. Compared with the photonic crystals pressure detection device designed by Suthar and Bhargava [21], which used sharp transmission peaks to achieve pressure detection of 0–6 GPa, and the 0–3 GPa pressure detection achieved by Dong et al. [44], the proposed JM has a wider pressure detection range (0–17.2 GPa) and better performance.

Multitasking sensor has become a research hot spot in the sensing field due to its advantages of functional integration and multiscenario application [44], which saves the cost of multiple single-function sensors to complete the task [44]. The proposed multitasking JM not only realizes the wide range of σ detection discussed above on the positive scale but also realizes high-precision cell distinction on the negative scale, reflecting the integration of functions.

Three types of normal human cells (GES-1, LO_2, and HEM) and their corresponding cancer ones (MGC-803, 7721, MEL) are shown in Table III [23]. At the same concentration (4.48×10^5 cells/mL), cancer cells generally have higher RI compared to normal ones, which is attributed to their larger cell nucleus, containing more proteins that help cells divide rapidly. Therefore, RI is an important identification indicator [23]. However, in Table III, the RI values corresponding to normal cells and cancer ones are 1.65998, 1.66013, 1.66034, 1.66104, 1.66069, and 1.66124, respectively [23]. The change of RI is accurate to 1×10^{-5} RIU, and the difference is very small, which presents a great challenge for various optical RI sensors in examining cancer cells. Next, the proposed JM has a resolution of up to 1×10^{-6} RIU to achieve a high-resolution distinction between normal cells and cancer ones.

Under the condition that the EWs of $f = 128.39$ THz propagate negatively into the JM, the JM can realize the high-resolution RI detection in the detection cavity RI (n_C) range of 1.6595–1.6615 by identifying the δ_+^H peak value. Fig. 7(a) is a 3-D diagram of the continuous change of the δ_+^H curve with the variation of n_C. It can be found that the δ_+^H peak is fixed at $\theta = 73.715°$, and within the detection range, $\delta_+^H > 3.09 \times 10^{-4}$ m, which facilitates experimental observation and measurement. To prove the high resolution of RI detection, Fig. 7(b) displays the change of δ_+^H peak value belonging to $n_C = 1.661499$ and $n_C = 1.6615$ when n_C varies by 1×10^{-6} RIU. $\Delta\delta_+^H = 2.9 \times 10^{-8}$ m and can be clearly observed after 10^4 times amplification by weak measurement technology [12]. Therefore, the JM has the advantage of distinguishing 1×10^{-6} RIU changes. Detection points in the range of $n_C = 1.6595$–1.661 are taken at equal intervals of 5×10^{-4} RIU, and Fig. 7(c) exhibits the linear fitting curve belonging to RI detection. The LFR of δ_+^H peak value and n_C is $\delta_+^H = 5.292 \times 10^{-2} n_C - 0.0875$. $S = 5.292 \times 10^{-2}$ m/RIU means that PSHE response to RI changes reaches the centimeter level, indicating that the RI detection of the JM is very sensitive and has excellent performance. $R^2 = 0.9919$ also demonstrates the reliability of LFR. The cell solution to be detected is injected into the detection cavity using a precision

technique [37]. Since the RI of the cells listed in Table III is all within the n_C detection range of 1.6595–1.6615, the JM can completely meet the detection and distinction of different cells. Fig. 7(d) shows the δ_+^H curves corresponding to the three normal cells and their cancer ones. It can be seen that the peak difference of δ_+^H separately belonging to MEL with the highest RI ($n_C = 1.66124$) and GES-1 with the lowest RI ($n_C = 1.65998$) is as high as $\Delta\delta_+^H = 6.51 \times 10^{-5}$ m, which is enough to prove that the JM is sensitive to changes in cells RI. In addition, since the δ_+^H peaks corresponding to the three cancer cells with higher RI are all larger than those of normal ones, the JM proposed provides a simple and rapid way to identify normal and cancer cells: at the concentration of 4.48×10^{-5} cells/mL, when the maximum δ_+^H value is larger than 3.7×10^{-4} m, it can be identified as cancer cells; otherwise, it is normal ones. Compared with the RI sensor that uses the local resonance optical tunneling effect to detect cancer cells with $S = 2.48 \times 10^{-5}$ m/mL and the resolution of 1×10^{-5} RIU [23], the JM designed with $S = 5.292 \times 10^{-2}$ m/RIU and resolution of 1×10^{-6} RIU has more excellent detection performance, which helps to provide efficient, sensitive, and accurate biomedical detection.

To systematically and intuitively demonstrate the advantages of the proposed JM, the correlatively previous sensors with excellent performance are listed in Table IV. Compared with the given JM, it can be seen that the designed JM integrates multiscale and multitasking and is generally better than previous sensors. In addition, the robustness of the JM is discussed in Section IV of the Supplementary Material. Therefore, the studied JM has a certain advanced nature and value.

IV. Conclusion

To sum up, a multiscale and multitasking JM based on PSHE is proposed in this article, which has the advantages of small size and compact structure, urgently needed for microsensor. Operating in the SWIR band, it has the advantages of high penetration depth, noninvasive, and real-time detection. When the EWs, respectively, propagate positively and negatively, the corresponding multitasking of pressure detection and RI biosensing is realized. On the positive scale, when there is air in the detection cavity, by identifying θ belonging to the δ_+^H peak, the pressure detection of 0–17.2 GPa can be realized by the JM with $S = 1.421°$/GPa, which has the advantage of wide range. When the detection cavity is injected with the cells solution, the biosensing in the RI range of 1.6595–1.6615 can be achieved by locking the δ_+^H peak value on the negative scale, whose high resolution of 1×10^{-6} RIU and high S of 5.292×10^{-2} m/RIU are one of the highlights in this article. By virtue of its wide pressure detection range, the designed JM can detect the change of large pressure exerted on it in real time during heavy industrial production. In addition, since the JM can realize all-optical biosensing in the SWIR range, in the field of biomedical sensing, the normal cells and corresponding cancer ones, which are injected into the detection cavity, can be noninvasively and contactlessly distinguished with a high resolution by the JM.

References

[1] K. Budidha, S. Chatterjee, M. Qassem, and P. A. Kyriacou, "Monte Carlo characterization of short-wave infrared optical wavelengths for biosensing applications," in *Proc. 43rd Annu. Int. Conf. IEEE Eng. Med. Biol. Soc. (EMBC)*, Nov. 2021, pp. 4285–4288.

[2] D. Ding et al., "X-ray-activated simultaneous near-infrared and short-wave infrared persistent luminescence imaging for long-term tracking of drug delivery," *ACS Appl. Mater. Interface*, vol. 13, no. 14, pp. 16166–16172, Apr. 2021.

[3] C.-W. Lin et al., "In vivo optical detection and spectral triangulation of carbon nanotubes," *ACS Appl. Mater. Interface*, vol. 9, no. 48, pp. 41680–41690, Dec. 2017.

[4] S. Huang et al., "Surface plasmon-enhanced short-wave infrared fluorescence for detecting sub-millimeter-sized tumors," *Adv. Mater.*, vol. 33, no. 7, Feb. 2021, Art. no. 2006057.

[5] S. Singh and G. L. Samuel, "Laser micromachining of semiconductor materials," in *Application of Lasers in Manufacturing*. Singapore: Springer, 2019, pp. 111–141.

[6] A. Bainbridge, K. Mamic, L. A. Hanks, F. Al-Saymari, A. P. Craig, and A. R. J. Marshall, "Resonant cavity enhanced photodiodes in the short-wave infrared for spectroscopic detection," *IEEE Photon. Technol. Lett.*, vol. 32, no. 21, pp. 1369–1372, Nov. 15, 2020.

[7] S. Liu, S. Chen, S. Wen, and H. Luo, "Photonic spin Hall effect: Fundamentals and emergent applications," *Opto-Electron. Sci.*, vol. 1, no. 7, 2022, Art. no. 220007.

[8] X. Ling et al., "Recent advances in the spin Hall effect of light," *Rep. Prog. Phys.*, vol. 80, no. 6, Mar. 2017, Art. no. 066401.

[9] K. Y. Bliokh, A. Niv, V. Kleiner, and E. Hasman, "Geometrodynamics of spinning light," *Nature Photon.*, vol. 2, no. 12, pp. 748–753, Dec. 2008.

[10] A. Aiello and J. P. Woerdman, "Role of beam propagation shifts," *Opt. Lett.*, vol. 33, no. 13, pp. 1437–1439, Jul. 2008.

[11] X. Zhou, X. Ling, H. Luo, and S. Wen, "Identifying graphene layers via spin Hall effect of light," *Appl. Phys. Lett.*, vol. 101, no. 25, pp. 1–10, Dec. 2012.

[12] O. Hosten and P. Kwiat, "Observation of the spin Hall effect of light via weak measurements," *Science*, vol. 319, no. 5864, pp. 787–790, Feb. 2008.

[13] V. A. Popescu, Y. K. Prajapati, and A. K. Sharma, "Highly sensitive magnetic field detection in infrared region with photonic spin Hall effect in silicon waveguide plasmonic sensor," *IEEE Trans. Magn.*, vol. 57, no. 10, pp. 1–10, Oct. 2021.

[14] A. Srivastava, A. K. Sharma, and Y. Kumar Prajapati, "On the sensitivity-enhancement in plasmonic biosensor with photonic spin Hall effect at visible wavelength," *Chem. Phys. Lett.*, vol. 774, Jul. 2021, Art. no. 138613.

[15] C. Wang, "Monitoring of the central blood pressure waveform via a conformal ultrasonic device," *Nat. Biomed. Eng.*, vol. 2, no. 9, p. 9, Sep. 2018.

[16] T. Q. Trung and N. Lee, "Flexible and stretchable physical sensor integrated platforms for wearable human-activity monitoringand personal healthcare," *Adv. Mater.*, vol. 28, no. 22, pp. 4338–4372, Jun. 2016.

[17] Y. Liu, M. Pharr, and G. A. Salvatore, "Lab-on-skin: A review of flexible and stretchable electronics for wearable health monitoring," *ACS Nano*, vol. 11, no. 10, pp. 9614–9635, Oct. 2017.

[18] Y. Zhu et al., "Highly sensitive and skin-like pressure sensor based on asymmetric double-layered structures of reduced graphite oxide," *Sens. Actuators B, Chem.*, vol. 255, pp. 1262–1267, Feb. 2018.

[19] C. Mahata, H. Algadi, J. Lee, S. Kim, and T. Lee, "Biomimetic-inspired micro-nano hierarchical structures for capacitive pressure sensor applications," *Measurement*, vol. 151, Feb. 2020, Art. no. 107095.

[20] R. B. Gowda, P. Sharan, and K. Saara, "1-dimensional silicon photonic crystal pressure sensor for the measurement of low pressure," *Results Opt.*, vol. 10, Feb. 2023, Art. no. 100352.

[21] B. Suthar and A. Bhargava, "Pressure sensor based on quantum well-structured photonic crystal," *Silicon*, vol. 13, no. 6, pp. 1765–1768, Jun. 2021.

[22] H. A. Elsayed, A. Sharma, Z. A. Alrowaili, and T. A. Taha, "Theoretical investigation of pressure sensing using a defect of polystyrene inside photonic crystals," *Mater. Chem. Phys.*, vol. 270, Sep. 2021, Art. no. 124853.

[23] A. Jian et al., "Enhancement of the volume refractive index sensing by ROTE and its application on cancer and normal cells discrimination," *Sens. Actuators A, Phys.*, vol. 313, Oct. 2020, Art. no. 112177.

[24] A. Ehyaee, M. Mohammadi, M. Seifouri, and S. Olyaee, "Design and numerical investigation of a dual-core photonic crystal fiber refractive index sensor for cancer cells detection," *Eur. Phys. J. Plus*, vol. 138, no. 2, pp. 1–7, Feb. 2023.

[25] S. Singh, A. K. Sharma, P. Lohia, D. K. Dwivedi, V. Kumar, and P. K. Singh, "Simulation study of reconfigurable surface plasmon resonance refractive index sensor employing bismuth telluride and MXene nanomaterial for cancer cell detection," *Phys. Scripta*, vol. 98, no. 2, Jan. 2023, Art. no. 025813.

[26] S. Chen, X. Ling, W. Shu, H. Luo, and S. Wen, "Precision measurement of the optical conductivity of atomically thin crystals via the photonic spin Hall effect," *Phys. Rev. Appl.*, vol. 13, no. 1, Jan. 2020, Art. no. 014057.

[27] J. Liu, K. Zeng, W. Xu, S. Chen, H. Luo, and S. Wen, "Ultrasensitive detection of ion concentration based on photonic spin Hall effect," *Appl. Phys. Lett.*, vol. 115, no. 25, pp. 1–12, Dec. 2019.

[28] W. Zhang, S. Lou, X. Wang, S. Yan, Z. Tang, and Z. Xing, "Multi-function sensor based on rectangular-lattice photonic crystal fiber with high pressure sensitivity," *Sens. Actuators A, Phys.*, vol. 310, Aug. 2020, Art. no. 111987.

[29] Y. Yu, Y. Chen, H. Hu, W. Xue, K. Yvind, and J. Mork, "Nonreciprocal transmission in a nonlinear photonic-crystal Fano structure with broken symmetry," *Laser Photon. Rev.*, vol. 9, no. 2, pp. 241–247, Jan. 2015.

[30] H. Wang and A. M. Rollins, "Generation of smooth continuum centered at 1.15 μm for ultrahigh resolution OCT," *Proc. SPIE*, vol. 6460, pp. 46–52, Mar. 2007.

[31] A. S. Kurkov, V. V. Dvoyrin, and A. V. Marakulin, "All-fiber 10 W holmium lasers pumped at λ=1.15 μm," *Opt. Lett.*, vol. 35, no. 4, pp. 490–492, Feb. 2010.

[32] M. Huang, "Stress effects on the performance of optical waveguides," *Int. J. Solids Struct.*, vol. 40, no. 7, pp. 1615–1632, Apr. 2003.

[33] S. Guo, C. Hu, and H. Zhang, "Ultra-wide unidirectional infrared absorber based on 1D gyromagnetic photonic crystals concatenated with general Fibonacci quasi-periodic structure in transverse magnetization," *J. Opt.*, vol. 22, no. 10, Sep. 2020, Art. no. 105101.

[34] A. H. Carim and A. Bhattacharyya, "Si/SiO_2 interface roughness: Structural observations and electrical consequences," *Appl. Phys. Lett.*, vol. 46, no. 9, pp. 872–874, May 1985.

[35] T. DiTommaso et al., "Cell engineering with microfluidic squeezing preserves functionality of primary immune cells in vivo," *Proc. Nat. Acad. Sci. USA*, vol. 115, no. 46, pp. 10907–10914, Nov. 2018.

[36] J. Tan, S. Sohrabi, R. He, and Y. Liu, "Numerical simulation of cell squeezing through a micropore by the immersed boundary method," *Proc. Inst. Mech. Eng., C, J. Mech. Eng. Sci.*, vol. 232, no. 3, pp. 502–514, Feb. 2018.

[37] F. Intonti et al., "Rewritable photonic circuits," *Appl. Phys. Lett.*, vol. 89, no. 21, Nov. 2006, Art. no. 211117.

[38] C. Gao and B. Guo, "Enhancement and tuning of spin Hall effect of light in plasma metamaterial waveguide," *Phys. Plasmas*, vol. 24, no. 9, Sep. 2017, Art. no. 093520.

[39] F. Amiripour, S. Ghasemi, and S. N. Azizi, "A novel non-enzymatic glucose sensor based on gold-nickel bimetallic nanoparticles doped aluminosilicate framework prepared from agro-waste material," *Appl. Surf. Sci.*, vol. 537, Jan. 2021, Art. no. 147827.

[40] H. Dai, L. Yuan, C. Yin, Z. Cao, and X. Chen, "Direct visualizing the spin Hall effect of light via ultrahigh-order modes," *Phys. Rev. Lett.*, vol. 124, no. 5, Feb. 2020, Art. no. 053902.

[41] B.-F. Wan, Y. Xu, Z.-W. Zhou, D. Zhang, and H.-F. Zhang, "Theoretical investigation of a sensor based on one-dimensional photonic crystals to measure four physical quantities," *IEEE Sensors J.*, vol. 21, no. 3, pp. 2846–2853, Feb. 2021.

[42] Y. Ma, P. Wang, and H. Zhang, "Investigation on a multiwindow spin Hall effect and its applications based on a periodic superconducting structure with evanescent waves," *J. Opt. Soc. Amer. B, Opt. Phys.*, vol. 38, no. 10, p. 2799, Oct. 2021.

[43] M. N. Baitha and K. Kim, "Polarization manipulation of giant photonic spin Hall effect using wave-guiding effect," *J. Appl. Phys.*, vol. 132, no. 5, Aug. 2022, Art. no. 053102.

[44] P. Dong, J. Cheng, H. Da, and X. Yan, "Controlling photonic spin Hall effect in graphene-dielectric structure by optical pumping," *New J. Phys.*, vol. 22, no. 11, Nov. 2020, Art. no. 113007.

[45] M. Danaie and B. Kiani, "Design of a label-free photonic crystal refractive index sensor for biomedical applications," *Photon. Nanostruct.-Fundam. Appl.*, vol. 31, pp. 89–98, Sep. 2018.

Jun-Yang Sui was born in Jiangsu, China, in 2002. He is currently pursuing the bachelor's degree with the Nanjing University of Posts and Telecommunications, Nanjing, China.

His main research interests include photonic crystals logic gate and sensing.

Jia-Hao Zou was born in Yixing, Jiangsu Province, China, in 2003. He is currently pursuing the bachelor's degree with the Nanjing University of Posts and Telecommunications, Nanjing, China.

His main research interests include photonic crystals logic gate and sensing.

Si-Yuan Liao was born in Jiangsu, China, in 2001. He is currently pursuing the bachelor's degree with the Nanjing University of Posts and Telecommunications, Nanjing, China.

His main research interests include absorber and polarization conversion.

Bao-Fei Wan was born in Jiangsu, China, in 1999. He is currently pursuing the master's degree with the Nanjing University of Posts and Telecommunications, Nanjing, China.

His main research interests include photonic crystal sensor and waveguide structure.

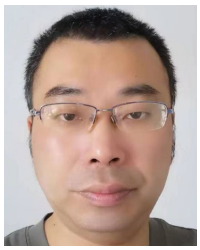

Hai-Feng Zhang was born in Jiangxi, China, in 1978. He received the M.Sc. degree in electronics science and technology from Nanchang University, Nanchang, China, in 2008, and the Ph.D. degree in the College of Electronic and Information Engineering, Nanjing University of Aeronautics and Astronautics, Nanjing, China, in 2014.

He is currently a Professor with the College of Electronic and Optical Engineering & College of Flexible Electronics (Future Technology), Nanjing University of Posts and Telecommunications, Nanjing. His main research interests include the computational electromagnetics, plasma photonic crystal, plasma stealthy electromagnetic, metastructure-based polarization converter, absorption, and its reconfigurable and optimized methods.